Southern Hemisphere Climate Variability Forced by Northern Hemisphere Ice Sheet Topography

T. R. Jones[1*], W. H. G. Roberts[2], E. J. Steig[3], K. M. Cuffey[4], B. R. Markle[3], J. W. C. White[5]

[1]Institute of Arctic and Alpine Research, University of Colorado, Boulder, CO 80309-0450, USA.

[2]Bristol Research Initiative for the Dynamic Global Environment and Bristol Glaciology Centre, School of Geographical Sciences, University of Bristol, Bristol BS8 1SS, United Kingdom

[3]Department of Earth and Space Sciences, University of Washington, Seattle, WA 98195-1310, USA.

[4]Department of Geography, University of California, Berkeley, CA 94720, USA.

[5]Institute of Arctic and Alpine Research and Department of Geological Sciences, University of Colorado, Boulder, CO 80309-0450, USA.

*corresponding author: Tyler Jones (tyler.jones@colorado.edu)

The presence of large Northern Hemisphere ice sheets and reduced greenhouse gas concentrations during the Last Glacial Maximum (LGM) fundamentally altered global ocean-atmosphere climate dynamics[1]. Model simulations and paleoclimate records suggest that glacial boundary conditions affected the El Niño-Southern Oscillation (ENSO)[2,3], a dominant source of short-term global climate variability. Yet, little is known about changes in short-term climate variability at mid-to high latitudes. Here, we use an ultra-high resolution water isotope record from West Antarctica to demonstrate that interannual to decadal climate variability at high southern latitudes was almost twice as large at the LGM compared to the Holocene. Climate model simulations indicate that this increased variability reflects an increase in the teleconnection strength between the tropical Pacific and West Antarctica, owing to a shift in the mean location of tropical convection. This shift, in turn, can be attributed to the influence of topography and albedo of the North American ice sheets on atmospheric circulation. As the planet deglaciated, the largest and most abrupt decline in teleconnection strength occurred between ~16 and 15 ka, followed by a slower decline into the early Holocene.

During glacial-interglacial transitions, the coupled ocean-atmosphere system shifts between stable states, driven by large climate forcings, including Milankovitch orbital cycles, greenhouse gas concentrations, and the decay of continental ice sheets[1]. The state changes are observed in paleoclimate proxy archives such as ice cores at high latitudes, and lake sediments and speleothems in the tropics and mid-latitudes. The state of the tropical Pacific is particularly important because this region plays a role in the generation and communication of climate anomalies between the low and high latitudes[4,5].

Whether the nature of ENSO changed between the Last Glacial Maximum (LGM) and the Holocene is an important question[3,6]. However, proxy studies of ENSO variability during the LGM remain contradictory[7,8], and the results of modeling studies are similarly ambiguous[2]. One obstacle to understanding past ENSO variability is disentangling changes in ENSO itself from changes in its influence on climate outside the tropics, i.e. the strength of ENSO-related teleconnections, which can vary over time[9].

Tropical Pacific climate variability is an important driver of interannual to multidecadal climate variability in West Antarctica[4,5]. Warm sea surface temperatures (SSTs) in the tropical Pacific drive the propagation of atmospheric

Rossby waves towards the high latitudes, affecting weather systems that develop over the Amundsen Sea[4,5]. Variability in the Amundsen Sea region dominates climate variability over the adjacent West Antarctic Ice Sheet (WAIS)[5,10,11]. Over longer timescales, the influence of tropical climate variability on the Amundsen Sea may have implications both for the stability of the ice sheet[12] and for the ventilation of CO_2 from the Southern Ocean[13].

The influence of tropical variability on West Antarctica climate is reflected in ice core records from the WAIS. In particular, oxygen and hydrogen isotope ratios of water are sensitive to temperature and atmospheric circulation anomalies associated with large ENSO events[14]. Such records might therefore yield important insights about changes in tropical climate variability and tropical-to-extratropical teleconnections during glacial-interglacial transitions. In this study, we utilize a high-resolution hydrogen isotope (δD) record from the WAIS Divide ice core (WDC) to investigate ~31 kyr of high-frequency climatic variability. The data were produced using laser absorption spectroscopy coupled with a continuous flow analysis system[15]. The record is the longest continuously-measured water isotope record ever recovered, with an effective sample resolution of 5 mm and a maximum difference in age between consecutive samples of 0.33 years.

We use spectral techniques (see Methods) on the WDC δD record to analyze West Antarctic climate variability (Fig. 1). Periods greater than 3 years are preserved throughout the 31 kyr record (Extended Data Fig. 1a). To account for attenuation of the δD signal by diffusion in the firn column and solid ice[16], we apply a diffusion correction on consecutive 500-yr data windows (see Methods; Extended Data Fig. 2c). We isolate the amplitude of 3-7 and 4-15 yr δD variations by averaging power density over these frequency ranges. The 3-7 yr range is typical of a high-frequency spectral peak seen in observations of the Southern Oscillation Index (SOI), while the 4-15 yr range is less affected by diffusion (Extended Data Fig. 1a) and captures the decadal variability observed in the SOI (Extended Data Fig. 1c), tropical Pacific coral isotope records[17], and in modern observations in West Antarctica[5,14].

We find that the mean amplitudes of the diffusion-corrected variability in the 3-7 and 4-15 yr bands are elevated in the Late Glacial (16-31 ka) relative to the Holocene (0-10 ka) (Fig. 1c,d). A ~50% decrease in amplitude occurs from ~16 to 10 ka in both time series. This decline occurs in two steps: an abrupt decrease at ~16 ka followed by a second but less pronounced decline from ~13-10 ka. Neither time series reveal other significant changes in

variability during the Holocene or during the Late Glacial. We use an objective algorithm (see Methods) to detect initial significant decline in the diffusion-corrected 4-15 yr time series based on 500-yr data windows (Extended Data Fig. 2a,b). We find that the decline began at 16.44 ka ±0.30 kyr (all ages are given relative to present = 1950 C.E.). Identical results are obtained using the 3-7 yr time series. The timing of the initial decline is robust among different detection techniques. Using a sub-set of 100-yr data windows for the diffusion-corrected 4-15 yr time series (Extended Data Fig. 2c,d), the decline occurs at 16.24 ka ±0.17 kyr. The timing of the decline is not an artifact of the diffusion correction. Using the raw data in the 4-15 yr band for 500-yr data windows (Fig. 1d), a ~40% decrease in amplitude occurs from ~16 to 10 ka, with initial significant decline occurring at 15.94 ka ±0.30 kyr. Conservatively, this places the decline in WDC variability between 16.74 to 15.64 ka, with a central estimate of 16.24 ka.

The climate shift at ~16 ka coincides with large-scale geologic events observed in proxy records across the globe. A substantial drawdown of the Laurentide Ice Sheet (LIS) surface is estimated to have occurred at 16 ka BP (from ^{14}C dating)[18], corresponding to the Heinrich Event 1 (H1) iceberg discharge event in the Northern Hemisphere (Fig. 2). The H1 ice rafted debris is of Laurentide origin[19], indicating abrupt changes in ice mass and the topography of the LIS at this time. The Cordilleran ice sheet also declined rapidly at this time[20], and the drawdown of the combined Laurentide-Cordilleran ice sheets (LCIS) has been suggested as a possible forcing mechanism for the transition from dry to wet conditions in Indonesia[21] (Fig. 2c). Taken together, the similarity in timing of these various records suggests a common link.

To investigate the mechanisms responsible for changing high-frequency variability at WDC, we use the HadCM3 fully-coupled ocean-atmosphere model to simulate climate in thousand-year steps from 28 to 0 ka[22] (see Methods). We assess variability in both the Amundsen Sea region and the tropical Pacific. Since the isotopic composition of ice at WDC is indicative of atmospheric circulation in the Amundsen Sea region[14] (Fig. 3a), we examine the mid-level flow in the model, represented by the 500 hPa height field. The amplitude of the simulated variability in the mean 500 hPa geopotential height field (Z_{ASL}) of the Amundsen Sea Low (ASL) region (*55-70°S, 195-240°E*) follows the same trend as the observations from WDC: more variability during the LGM, less variability during the Holocene, and a decline in variability at 16 ka (Fig. 4a). We examine the tropical Pacific influence (Z_{pac}) on the

99 modeled Z_{ASL} by linearly removing the effect of the basin-wide (*150-270°E, 5°N-5°S*) tropical Pacific SST (SST_{pac})
100 from the Z_{ASL} time series (Fig. 4e,f). The amplitude of the residual ASL variability is essentially constant for the last
101 28 kyr (Fig. 4a), demonstrating that the change in the ASL is connected to tropical variability.
102
103 The increased Z_{ASL} variability at the LGM could be the result of either increased tropical variability or a change in
104 efficiency of the tropical-high latitude teleconnection, forced by a change in the tropical mean state. To separate
105 these processes, we compute the strength of the teleconnection between the tropics and ASL by constructing
106 composite maps. These composites show the average response of the 500 hPa geopotential height field to ENSO
107 events in the tropical Pacific (see Methods). We use a composite that imposes both an upper and lower limit on the
108 size of SST_{pac} (± 1.25 to 2.5 times the pre-industrial standard deviation) to eliminate the possible influence of
109 stronger or weaker ENSO events during the glacial period. Composites with or without this upper limit are
110 indistinguishable. The results demonstrate that, in our HadCM3 experiments, the change in Z_{ASL} variability is the
111 result of a more efficient teleconnection, rather than a change in ENSO variability (see Methods). A time series of
112 the strength of the teleconnection over the last 28 ka (Fig. 2a, 4b) shows that the teleconnection is stronger through
113 the LGM until 16 ka, at which time it rapidly decreases. This is in agreement with the modeled change in variability
114 in Z_{ASL} and the observed timing of change in the WDC record. A change in the LGM teleconnection strength is also
115 evident in eight out of eleven of the PMIP2/3 models (Extended Data Fig. 7). This is remarkable given the diversity
116 of the response of these models' tropical climate to LGM forcing[23].
117
118 The stronger teleconnection in the glacial period in our simulations suggests a change in the tropical Pacific mean
119 state. Such a change could result from the lowered GHG concentrations, the altered orbital forcing, or the presence
120 of continental ice sheets. In HadCM3, we test each of these boundary conditions individually to evaluate their
121 impact (see Methods). The GHG concentrations and orbital forcing cause a negligible change, whereas the influence
122 of continental ice sheets is significant. Two processes associated with continental glaciation may be important for
123 changing the teleconnection: the lowering of sea level leading to the exposure of the shelf seas in the West
124 Pacific[23,24], and the topographic and albedo forcing of the LCIS. When considered separately, the lowered sea level
125 causes a small change in the teleconnection that is statistically significant only to the north of the ASL region (Fig.

3e). Since flooding of West Pacific shelf seas is thought to have occurred at ~13 ka[21], this may be a possible cause of the ~13-10 ka decline in WDC variability, but cannot explain the larger step change at ~16 ka.

The topography and albedo of the LCIS force a large change to the teleconnection strength at ~16 ka, which is statistically significant across the ASL region (Fig. 3d). This timing is consistent with major deglacial changes in the LCIS, including its drawdown[18]. To separate the effects of topography and albedo, we perform two tests. First, using pre-industrial settings, we introduce only the LGM-LCIS into the model. In this case we find that almost the full LGM teleconnection strength change is realized (Fig. 3d). Second, we remove the LGM-LCIS topographic effect, while keeping the albedo effect. Here, the teleconnection pattern changes, but is not significant in the ASL region. Our results therefore demonstrate a link between the topography of the LCIS and multi-year to decadal climate variations in West Antarctica – a previously undocumented inter-polar teleconnection mechanism.

When the LCIS surface is high, the circulation in the North Pacific changes, with a persistent annual mean Aleutian Low that is deeper and farther south, a response that is consistent amongst climate models[25]. This weakens the mean winds in the West Pacific, causing the warm pool to expand eastward, as occurs during an El Niño event. The atmospheric convection moves with the warmer waters away from the Maritime Continent (Fig. 4c); hence, rainfall decreases in this region, consistent with the LGM drying inferred from lake sediments in Indonesia[21] (Fig. 2c) and stalagmites in Borneo[26] (Fig. 2d). The shifted convection then causes a change in the location of the atmospheric heating that occurs during ENSO events. Changing the location of this heating alters the structure of the extra-tropical Rossby waves that are excited during ENSO events, so that, when the LCIS is present, there are additional circulation anomalies in the Southern Hemisphere high latitudes. There are large changes in how the Rossby waves are forced from the tropics, but no change in how they propagate to the Southern Hemisphere. Since Rossby waves are the primary mechanism responsible for the tropical Pacific-West Antarctic teleconnection[4,5], the LCIS can force a change in West Antarctic climate variability. Hence, when an ENSO event occurs during the LGM – even if it is no bigger than during the modern era – it has a larger impact on West Antarctic climate than it does during the Holocene.

Our results identify a novel influence of Northern Hemisphere ice sheet topography on the climate system. By altering the coupled ocean-atmospheric circulation, the decay of the LCIS affected the strength of interactions between the tropical Pacific and high southern latitudes, reducing interannual and decadal variability in West Antarctica by nearly half. While several abrupt climate events occur during the last 31 kyr, including Dansgaard-Oeschger events, the Bølling-Allerød, the Younger Dryas, and melt water pulse 1a[24,27] (Fig. 2e,f), the interannual and decadal climate variability in West Antarctica and the patterns of rainfall in the tropical west Pacific do not appear to be affected. Instead, the initial reduction in West Antarctic variability at ~16 ka corresponds to a maximum in North Atlantic ice rafted debris layers during H1[18]. It was this ice sheet purge that likely reduced LCIS topography beyond a critical threshold, altering the inter-hemispheric climate dynamics of the Pacific basin, even as separate abrupt climate events continued to occur in the Atlantic basin and further afield.

References

1. Broecker, W. S. & Denton, G. H. The role of ocean-atmosphere reorganizations in glacial cycles. *Geochimica et Cosmochimica Acta* **53,** 2465–2501 (1989).

2. Zheng, W., Braconnot, P., Guilyardi, E., Merkel, U. & Yu, Y. ENSO at 6ka and 21ka from ocean–atmosphere coupled model simulations. *Clim Dyn* **30,** 745–762 (2007).

3. Tudhope, A. W. *et al.* Variability in the El Niño-Southern Oscillation through a glacial-interglacial cycle. *Science* **291,** 1511–1517 (2001).

4. Lachlan-Cope, T. & Connolley, W. Teleconnections between the tropical Pacific and the Amundsen-Bellinghausens Sea: Role of the El Niño/Southern Oscillation. *Journal of Geophysical Research: Atmospheres* **111,** (2006).

5. Ding, Q., Steig, E. J., Battisti, D. S. & Küttel, M. Winter warming in West Antarctica caused by central tropical Pacific warming. *Nature Geoscience* **4,** 398–403 (2011).

6. Turney, C. S. M. *et al.* Millennial and orbital variations of El Niño/Southern Oscillation and high-latitude climate in the Last Glacial Period. *Nature* **428,** 306–310 (2004).

7. Sadekov, A. Y. *et al.* Palaeoclimate reconstructions reveal a strong link between El Niño-Southern Oscillation and tropical Pacific mean state. *Nature Communications* **4,** L11704 (2013).

8. Ford, H. L., Ravelo, A. C. & Polissar, P. J. Reduced El Nino-Southern Oscillation during the Last Glacial Maximum. *Science* **347,** 255–258 (2015).

9. Merkel, U., Prange, M. & Schulz, M. ENSO variability and teleconnections during glacial climates. *Quaternary Science Reviews* **29,** 86–100 (2010).

10. Steig, E. J. *et al.* Warming of the Antarctic ice-sheet surface since the 1957 International Geophysical Year. *Nature* **457,** 459–462 (2009).

11. Nicolas, J. P. & Bromwich, D. H. Climate of West Antarctica and influence of marine air intrusions*. *Journal of Climate* **24,** 49–67 (2011).

12. Steig, E. J., Ding, Q., Battisti, D. S. & Jenkins, A. Tropical forcing of Circumpolar Deep Water Inflow and outlet glacier thinning in the Amundsen Sea Embayment, West Antarctica. *Annals of Glaciology* **53,** 19–28 (2012).

13. Anderson, R. F. *et al.* Wind-driven upwelling in the Southern Ocean and the deglacial rise in atmospheric CO2. *Science* **323,** 1443–1448 (2009).

14. Steig, E. J. *et al.* Recent climate and ice-sheet changes in West Antarctica compared with the past 2,000 years. *Nature Geoscience* **6,** 372–375 (2013).

15. Jones, T. R. *et al.* Improved methodologies for continuous-flow analysis of stable water isotopes in ice cores. *Atmospheric Measurement Techniques* **10,** 617–632 (2017a).

16. Jones, T. R. *et al.* Water isotope diffusion in the WAIS Divide ice core during the Holocene and last glacial. *Journal of Geophysical Research: Earth Surface* **122,** 290–309 (2017b).

17. Urban, F. E., Cole, J. E. & Overpeck, J. T. Influence of mean climate change on climate variability from a 155-year tropical Pacific coral record. Nature **407**, 989–993 (2000).

18. Stern, J. V. & Lisiecki, L. E. North Atlantic circulation and reservoir age changes over the past 41,000 years. *Geophysical Research Letters* **40,** 3693–3697 (2013).

19. Dyke, A. S. *et al.* The Laurentide and Innuitian ice sheets during the Last Glacial Maximum. *Quaternary Science Reviews* **21,** 9–31 (2002).

20. Porter, S. C. & Swanson, T. W. Radiocarbon age constraints on rates of advance and retreat of the Puget Lobe of the Cordilleran Ice Sheet during the last glaciation. *Quaternary Research* **50,** 205–213 (1998).

21. Russell, J. M. *et al.* Glacial forcing of central Indonesian hydroclimate since 60,000 y BP. *Proceedings of the National Academy of Sciences* **111,** 5100–5105 (2014).

22. Singarayer, J. S. & Valdes, P. J. High-latitude climate sensitivity to ice-sheet forcing over the last 120kyr. *Quaternary Science Reviews* **29,** 43–55 (2010).

23. DiNezio, P. N. & Tierney, J. E. The effect of sea level on glacial Indo-Pacific climate. *Nature Geoscience* **6,** 485–491 (2013).

24. Deschamps, P. *et al.* Ice-sheet collapse and sea-level rise at the Bølling warming 14,600 years ago. *Nature* **483,** 559–564 (2012).

25. Yanase, W. & Abe-Ouchi, A. A numerical study on the atmospheric circulation over the midlatitude north Pacific during the Last Glacial Maximum. *Journal of Climate* **23,** 135–151 (2010).

26. Partin, J. W., Cobb, K. M., Adkins, J. F., Clark, B. & Fernandez, D. P. Millenial-scale trends in west Pacific warm pool hydrology since the Last Glacial Maximum. Nature 449, 452–455 (2007).

27. Johnsen, S. J. *et al.* Oxygen isotope and palaeotemperature records from six Greenland ice-core stations: Camp Century, Dye-3, GRIP, GISP2, Renland and NorthGRIP. *Journal of Quaternary Science* **16,** 299–307 (2001).

28. Waelbroeck, C. *et al.* Sea-level and deep water temperature changes derived from benthic foraminifera isotopic records. *Quaternary Science Reviews* **21,** 295–305 (2002).

29. Hemming, S. R. Heinrich events: massive Late Pleistocene detritus layers of the North Atlantic and their global climate imprint. *Reviews of Geophysics* **42,** 725 (2004).

30. Peltier, W. R. Global glacial isostasy and the surface of the ice-age Earth: the ICE-5G (VM2) model and GRACE. *Annu. Rev. Earth Planet. Sci.* **32**, 111–149 (2004).

Supplementary Information is available in the online version of the paper.

Acknowledgements

This work was supported by US National Science Foundation (NSF) grants 0537593, 0537661, 0537930, 0539232, 1043092, 1043167, 1043518, and 1142166. Field and logistical activities were managed by the WAIS Divide Science Coordination Office at the Desert Research Institute, Reno, NE, USA and the University of New Hampshire, USA (NSF grants 0230396, 0440817, 0944266, and 0944348). The National Science Foundation Division of Polar Programs funded the Ice Drilling Program Office (IDPO), the Ice Drilling Design and Operations (IDDO) group, the National Ice Core Laboratory (NICL), the Antarctic Support Contractor, and the 109th New York Air National Guard. W.H.G.R. was funded by a Leverhulme Trust Research Project Grant. All HadCM3 model simulations were carried out using the computational facilities of the Advanced Computing Research Centre, University of Bristol (http://www.bris.ac.uk/acrc/). We wish to thank Paul J. Valdes and Joy S. Singarayer for providing their model simulations, as well as the groups that provided climate model data as part of the PMIP2/3.

Author Contributions

T.R.J., W.H.G.R., and E.J.S. designed the project and led the writing of the paper. T.R.J., J.W.C.W., E.J.S., and B.R.M. contributed water isotope measurements. W.H.G.R. conducted HadCM3 simulations and led model analysis. T.R.J., K.M.C., E.J.S., and J.W.C.W. developed the diffusion-correction calculations. B.R.M. contributed change point detection algorithms and power density ratio calculations. All authors discussed the results and contributed input to the manuscript.

Author Information

Reprints and permissions information is available at www.nature.com/reprints. The authors declare no competing financial interests. Readers are welcome to comment on the online version of the paper. Correspondence and requests for materials should be addressed to T.R.J. (tyler.jones@colorado.edu).

Methods

1 Water isotope data

The WDC water isotope record (Fig. 1a) was analyzed on a continuous flow analysis (CFA) system[15] using a Picarro Inc. cavity ring-down spectroscopy (CRDS) instrument, model L2130-i. The data are reported in delta notation relative to Vienna Standard Mean Ocean Water (VSMOW, $\delta^{18}O = \delta D = 0‰$), normalized to Standard Light Antarctic Water (SLAP, $\delta^{18}O = -55.5‰$, $\delta D = -428.0‰$) scale. WDC is annually dated, with accuracy better than 0.5% of the age between 0-12 ka, and better than 1% of the age between 12-31 ka[31,32].

2 Frequency domain analyses

2.1 Spectral conversion

We use the MultiTaper method fast Fourier transform technique to calculate spectral power densities[33,34] of the measured water isotope time series. Similar to other paleoclimate studies[35], we use the pmtm.m routine of P. Huybers (http://www.people.fas.harvard.edu/~phuybers/Mfiles/). Before spectral analysis, the isotope data are linearly interpolated at a uniform time interval of 0.05 yr.

2.2 High-frequency signal attenuation

High-frequency water isotope information in ice cores is attenuated by diffusion in the firn column and deep ice[16,36,37,38,39,40]. Frequency spectra reveal the amount of signal attenuation as declines in the amplitude of a given frequency through time, relative to lower frequencies (Extended Data Fig. 1a). For WDC, the annual signal (1 yr) is indiscernible at ages >14 ka. The 2 yr signal is indiscernible from 17-19 ka. Signals >3 yr are detectable throughout the last 31 kyr, while signals >4 yr are not substantially attenuated by diffusion (Extended Data Fig. 1a).

2.3 Gaussian determination of diffusion lengths

The quantitative effects of diffusion can be represented by the convolution of a Gaussian filter with the original water-isotope signal deposited at the surface and subsequently strained by ice deformation and firn compaction[36,39] (Extended Data Fig. 1b). The power density spectrum observed in the ice core record (P(f)), after diffusion, is $P(f) = P_o(f) \exp[-(2\pi f \sigma_z)^2]$, where $P_o(f)$ represents the power spectrum of the undiffused signal, f is the

frequency $\frac{1}{\lambda}$, λ the signal wavelength, z the depth, and σ_z the diffusion length. Fitting a Gaussian to P(f) defines a standard deviation, σ_f , with units of 1/meters. The conversion $\sigma_z = \frac{1}{2\pi\sqrt{2}} \cdot \frac{1}{\sigma_f}$ then yields the diffusion length σ_z in units of meters[16]. The diffusion length expressed in units of time is $\sigma_t = \frac{\sigma_z}{\lambda_{avg}}$, where λ_{avg} is the mean annual layer thickness (m/yr) at a given depth (Extended Data Fig. 2c). The diffusion length quantifies the statistical vertical displacement of water molecules from their original position in the ice sheet. In the present study, we use our previously published WDC diffusion lengths, calculated for 500-yr data windows through the interval 0 – 29 ka[16].

2.4 Natural log determination of diffusion length

The σ_f variable can also be determined by using the slope of the linear regression of ln(P(f)) vs. f^2. This provides a means of estimating diffusion-length uncertainty[16]. Here, $\sigma_f = \sqrt{\frac{1}{2 \cdot |(m_{ln})|}}$, where m_{ln} is the slope of the linear regression over the interval from 0.01 cycles^2/m^2 to the value at which systematic noise from the ice core analysis system overwhelms the physical signal. The point where noise dominates appears as a "kink" or "bend" in the decay of ln(P(f)). A maximum and minimum slope is fit within the standard deviation of the linear regression to determine an uncertainty range for σ_f.

2.5 Power density diffusion correction

Diffusion of a water isotope signal in an ice sheet reduces the power of high-frequencies, so P(f) takes the form of quasi-red noise. Given that WDC Holocene spectra show constant power density in the frequencies largely unperturbed by diffusion (periods >4 yrs), we use a white-noise normalization to estimate the original, pre-diffusion power density spectrum. Specifically, we calculate $P_o(f) = \mathrm{P} \exp(4\pi^2 f^2 \sigma_t^2)$, where P is the observed power density (per mil^2·yr), f the frequency (1/yr), and σ_t the diffusion length (yr). We report the average power density for the diffusion-corrected 3-7 and 4-15 yr bands calculated as the integral of power density divided by the frequency range. The uncertainty on these power density diffusion corrections is determined using the uncertainty range for diffusion lengths discussed in section 2.4.

3 Change point detection

We fit linear regressions to blocks of data centered on every possible point within the 3-7 and 4-15 yr relative amplitude time series, using block sizes of 2,500 to 10,000 yrs. We calculate the *p*-value for the *F*-test to determine whether the slope of the regression of each block is statistically different than zero (Extended Data Fig. 2b). We make no *a priori* assumptions about the timing or size of significant change and take an *a posteriori* confidence level equivalent to 95%: $\alpha = 1 - 0.95^{1/n}$, where n is the number of statistical test realizations[31]. The first significant change occurs at 16,440 ka for the 4-15 yr diffusion-corrected data (all ages are given relative to present = 1950 C.E.). The 3-7 yr diffusion-corrected data yields identical results. The first significant change in the 4-15 yr raw data (not corrected for diffusion) occurs at 15,940 yrs.

Uncertainty in the timing of initial change includes the spectral window resolution of 500-yrs (±250 yrs) and the WDC14 age scale (±1% for ages >12 ka[32]). For initial change centered at 16.4 ka and 15.9 ka, the age scale imposes an uncertainty of ±164 yrs and ±159 yrs, respectively. Adding the above in quadrature yields initial timing uncertainties of just less than ±300 yrs. We also estimate the change point visually using a sub-set of 4-15 yr diffusion-corrected data, calculated using 100-yr non-overlapping windows between ~16.64 and 15.54 ka. The change occurs at 16.24 ka, with uncertainty on the window length of ± 50 yrs and a dating uncertainty of ±162 yrs. Added in quadrature, this gives an uncertainty value of ± 170 yrs.

4 HadCM3 model simulations

4.1 Model setup

We use the fully coupled ocean-atmosphere model HadCM3[41,42]. This model has been shown to simulate the climate in the tropical Pacific very well, including in its response to glacial forcing[23]. We simulate the climate over the last 28 ka in a series of snapshots run every 1 kyr[22]. For each snapshot, we prescribe the orbital forcing[43], greenhouse gas (GHG) concentration[44,45], and ice sheet topography and sea level[30]. We use a suite of simulations to test the sensitivity of the model to individual boundary conditions, including *Full 28-0 ka, Full 21 ka, 21 ka orbit + GHG, 21 ka ice sheets, LCIS albedo + topography* (where LCIS is the combined Laurentide-Cordilleran ice sheets)*, 21 ka West Pacific shelf exposure,* and *LCIS albedo.* Each of these simulations is defined in the Supplementary Information Data spreadsheet. All simulations are run for at least 500 years with analysis made on the final 200 years of each simulation.

363

364 **4.2 Amundsen Sea Low variability**

365 **4.2.1 Long-term evolution**

366 The variability in the WDC water isotope record on interannual and longer timescales is related to changes in the
367 large-scale atmospheric circulation, particularly in the Amundsen Sea Basin[14] (Fig. 3a). These changes in the
368 circulation can be characterized by the Amundsen Sea Low (ASL)[46,47]. To assess the amount of variability in the
369 ASL, we compute an *ASL index* of monthly mean 500 hPa height averaged from 55°-70°S and 195°-240°E (Z_{ASL}).
370 We use a 4-15 yr band-pass filter to isolate variability on the same timescale as the WDC record. Extended Data
371 Figure 3 shows the variance of Z_{ASL} within each 1 kyr snapshot, using the *Full 28-0 ka* simulations. From 28 ka until
372 around 15 ka, the ASL is more variable than during the Holocene (95% significant, F-test). Both the magnitude and
373 timing of the decrease are comparable to those observed in the WDC water isotope record.

374

375 **4.2.2 Internal *vs.* forced variability**

376 To assess how much of the change in the simulated Z_{ASL} is due to the tropics, we linearly remove the average of SST
377 across *5°N-5°S* and *150-270°E* (SST_{pac}) from the Z_{ASL}. This operation is performed by regressing Z_{ASL} onto SST_{pac},
378 as shown by the equation $Z_{pac} = SST_{pac} * regress(SST_{pac}, Z_{ASL})$. We then subtract Z_{pac} from Z_{ASL} to obtain the
379 component of Z_{ASL} that is unrelated to the tropical Pacific: $Z_{local} = Z_{ASL} - Z_{pac}$. The variance of Z_{local} is plotted in
380 Extended Data Figure 3. The results show that there is no statistically significant change in the ASL variability that
381 is unrelated to tropical Pacific SST over the deglaciation (95% significant, F-test). We compare these results,
382 obtained with 4-15 yr band pass filtered data of monthly mean model output, to annual mean data with no filtering
383 (Extended Data Fig. 3a,b). We obtain very similar results for both outputs. The tests described below use the annual
384 mean data.

385

386 **4.3 The tropical Pacific-to-ASL teleconnection**

387 The tropical Pacific-to-ASL teleconnection has been well documented[48,49]. To show this teleconnection in HadCM3,
388 we construct composite maps of 500 hPa height for years when the annual SST_{pac} anomaly exceeds ± 0.81 °C
389 (Extended Data Fig. 4). This threshold is chosen so that SST_{pac} anomalies exceed 1.25 standard deviations in a pre-
390 industrial simulation. We include cold ENSO events by multiplying the 500 hPa height field by (–1). Note that

391 computing SST_{pac} over the entire tropical Pacific basin eliminates biases that may arise from changes in the pattern
392 of SST variability, either in response to forcing or as a result of intrinsic ENSO variability.
393
394 The pre-industrial composite pattern that we obtain for the atmospheric response to tropical Pacific SST shows
395 greatest amplitude in the Amundsen Sea region, with a positive height anomaly for warm ENSO events (Extended
396 Data Fig. 4a). A similar pattern is obtained from reanalysis data using either regression analysis[48] or
397 compositing[48,50]. The composite is statistically significant across the Southern Hemisphere.
398
399 Using HadCM3, we find a similar composite pattern for the pre-industrial (Extended Data Fig. 4a) and *Full 21 ka*
400 (Extended Data Fig. 4b). The difference between the two patterns is shown in Extended Data Figure 4c; a Rossby-
401 wave response emanating from the western tropical Pacific is evident. This response is consistent with other studies
402 that show the tropical Pacific-to-ASL teleconnection[4,5,48,51]. Using each snapshot in the *Full 28-0 ka* simulations, we
403 evaluate the amplitude of the tropical Pacific-to-ASL teleconnection as the mean of the composite averaged over *55-*
404 *70°S* and *195-240°E* (Extended Data Fig. 5). There is a dramatic decrease in the strength of the teleconnection
405 around 16 ka.
406
407 **4.4 Teleconnection changes resulting from ENSO changes**
408 **4.4.1 Results from HadCM3 experiments**
409 We find that the simulated variance of SST_{pac} anomalies at 21 ka (σ=0.78°C) is increased by 40% compared to the
410 pre-industrial (σ=0.65°C). To determine the effect of SST variability on the teleconnection strength, we re-compute
411 the composites using SST_{pac} anomalies in the range $\pm$ 0.81°C < SST_{pac} < $\pm$ 1.63°C, corresponding to SST_{pac} at 0 ka
412 of $\pm$ 1.25σ to $\pm$ 2.5σ. By imposing both an upper and lower bound, the atmospheric response in the 500 hPa height
413 composites is unaffected by the amplitude of simulated ENSO events. Furthermore, any change in the frequency of
414 ENSO events is rendered unimportant by taking an average composite of events.
415
416 The composite patterns for all simulations from 28 ka to 0 ka, as well as their difference with the pre-industrial, are
417 unchanged by imposing the upper and lower bound, while the amplitude of the composites is slightly reduced. For
418 the *Full 21 ka simulation*, the average amplitude of the Z_{ASL} is 32 m without the upper bound, and 30 m with the

upper bound imposed (Extended Data Fig. 6). Therefore, even though HadCM3 simulates an increase in the strength of ENSO during the LGM, this is not the primary cause for the change in Z_{ASL} variability. Rather, the increased Z_{ASL} variability occurs because the atmospheric response to SST_{pac} during the glacial period is stronger than during the pre-industrial.

4.4.2. Results from Paleoclimate Model Intercomparison Project

For a subset of PMIP2/3 simulations (those for which sufficient data was available[52]), we follow the same procedure as outlined above to construct composites of 500 hPa height response to SST_{pac} anomalies. We include both the lower and upper SST_{pac} bounds. The composites are computed for pre-industrial and the *Full 21 ka* simulations (Extended Data Fig. 7). A change in the tropical Pacific-to-ASL teleconnection is apparent in many of the models. Since each model has a different teleconnection in the pre-industrial, the response of the models to 21 ka boundary conditions is also different.

At 21 ka, PMIP2/3 models with enhanced SST_{pac} variance do not display a consistently different teleconnection compared to models with reduced SST_{pac} variance. This confirms that changes in the tropical Pacific-to-ASL teleconnection strength are not driven by changes in the amplitude of SST_{pac} anomalies (i.e. ENSO). Indeed, in comparison to HadCM3, the most similar change in the teleconnection occurs in FGOALS-1.0g simulations. FGOALS-1.0g shows a large decrease in ENSO strength at 21 ka, compared to the HadCM3 increase. The FGOALS-1.0g positive geopotential height anomaly is shifted eastward, consistent with the location of the regional low-pressure center in the pre-industrial simulations.

4.5 Boundary condition changes responsible for the teleconnection change

In *Full 21 ka* simulations, a number of the climate forcings are changed significantly compared to the pre-industrial. These include insolation, the greenhouse gas (GHG) concentrations, and the size of the ice sheets (Extended Data Fig. 8a). We investigate the impact of each of these boundary condition changes on the teleconnection. The *21 ka orbit + GHG* simulation does not cause a significant change (Extended Data Fig. 8b). In the *21 ka ice sheets* simulation, which includes reduced sea level, enhanced albedo in the higher latitudes, and altered topography over North America and Europe, there is a large change in the amplitude of the teleconnection (Extended Data Fig. 8c).

447 Prior modeling simulations have explored other aspects of the topographic effects of Northern Hemisphere ice
448 sheets[53], including their influence on glacial climate[54], abrupt glacial climate change[55], the Atlantic Meridional
449 Overturning Circulation[56], and Heinrich Events[57].
450
451 The *LCIS albedo + topography* simulation displays a significant change in the teleconnection strength, similar in
452 magnitude to the *Full 21 ka* simulation (Extended Data Fig. 8e). The *LCIS albedo* simulation (i.e. albedo only)
453 displays a statistically significant change in the teleconnection, but its effect is much smaller than that of topography
454 and albedo combined (Extended Data Fig. 8f). Although we cannot isolate the effect of topography alone, our results
455 suggest topography is the dominant mechanism acting to change the teleconnection strength. This agrees with the
456 WDC shift in variability at ~16 ka, which is concurrent with the abrupt lowering of the LCIS[18].
457
458 It has been proposed that lowered sea level in the West Pacific at the LGM can have a large impact on tropical
459 Pacific climate by exposing the continental shelves[23,58]. We test this by changing only the land-sea mask in the West
460 Pacific in the *21 ka West Pacific shelf exposure* simulation (Extended Data Fig. 8d). This results in a change to Z_{ASL}
461 that is 3 to 4 times smaller than that seen in *LCIS albedo + topography* simulation. There is also a statistically
462 significant change in the composite map to the north of the ASL. In the WDC diffusion-corrected variability (3-7
463 and 4-15 yr bands), there appears to be a step-change that occurs at ~13 ka. This timing is consistent with the
464 flooding of the continental shelves in the West Pacific[24,59]. Therefore, it is possible that the WDC data is detecting
465 flooding of the continental shelves, but this effect is secondary to the abrupt change at ~16 ka.
466
467 **4.6 Climatic changes associated with the teleconnection change**
468 The tropical Pacific-to-ASL teleconnection can be considered as a Rossby Wave response to diabatic heating in the
469 western tropical Pacific[60]. The location of this diabatic heating will depend upon the mean state. To understand how
470 the mean state changes, we analyze how the patterns of precipitation and SST change in the 21 ka simulations
471 relative to the pre-industrial. Extended Data Figure 9a shows the precipitation difference between the *Full 21 ka*
472 simulation and the pre-industrial. There is a prominent decrease in precipitation over the Maritime Continent, and an
473 increase in precipitation over the Indian Ocean and the west and central tropical Pacific. This is consistent with
474 proxy evidence[21,23,61,]. In Extended Data Figure 9b, the 2*1 ka ice sheets* simulation accounts for the majority of the

precipitation changes in the *Full 21 ka* simulation. When we decompose this effect, the *LCIS albedo + topography* simulation accounts for most of the precipitation changes in the west and central tropical Pacific (Extended Data Fig. 9c), while the *21 ka West Pacific shelf exposure* simulation accounts for most of the precipitation changes over the Maritime Continent and in the Indian Ocean (Extended Data Fig. 9d). We find that there is a much larger change in West Pacific diabatic heating (as shown by the precipitation field) in the *LCIS albedo + topography* simulation than in the *21 ka West Pacific shelf exposure* simulation. Since the ASL responds to diabatic heating anomalies in the West Pacific, rather than the Indian Ocean, this is consistent with our interpretation that the LCIS dominates the tropical Pacific-to-ASL teleconnection strength change. The timing of the change in the precipitation pattern is shown in Fig. 4c. At 16 ka, the location of the tropical precipitation moves westward from its glacial position to its pre-industrial position in the far west Pacific.

The location of diabatic heating is ultimately a response to the winds and SST. Extended Data Fig. 9 shows that the SST patterns for the *Full 21 ka, 21 ka ice sheets, and LCIS albedo + topography* simulations are all similar. Although the global mean SST is much cooler in the *Full 21 ka* simulation (Extended Data Fig. 9a), it is the spatial structure of the SST that determines the climatic response[62]. Thus it is not surprising that all three simulations alter the teleconnection in a similar way. Furthermore, the SST pattern is consistent across most of the 21 ka PMIP2/3 simulations, indicating a robust SST response to an ice sheet. The SST pattern in the *Full 21 ka* simulation is associated with cyclonic flow in the North Pacific that is forced by the presence of the LCIS. Prior modeling has shown that this wind response to the LCIS could result from a summertime weakening of the sub-tropical high and a wintertime deepening of the Aleutian Low[62].

5 Data availability

The WDC water isotope data that support the findings of this study are available at http://gcmd.gsfc.nasa.gov/search/Metadata.do?entry=NSF-ANT10-43167#metadata. Additional supporting data, including model results, are provided in the Supplementary Information Data spreadsheet and the Extended Data.

Methods References

31. WAIS Divide Project Members. Onset of deglacial warming in West Antarctica driven by local orbital forcing. Nature 500, 440–444 (2013).

32. Sigl, M. *et al.* The WAIS Divide deep ice core WD2014 chronology – Part 2: annual-layer counting (0–31 ka BP). *Climate of the Past* **12,** 769–786 (2016).

33. Thomson, D. J. Spectrum estimation and harmonic analysis. *Proceedings of the IEEE* **70,** 1055–1096 (1982).

34. Percival, D. B., & Walden, A. T. *Spectral Analysis for Physical Applications*, 583 pp., Cambridge Univ. Press, New York (1993).

35. Markle, B. R. *et al.* Global atmospheric teleconnections during Dansgaard–Oeschger events. *Nature Geoscience* **10,** 36–40 (2017).

36. Johnsen, S. J., Stable isotope homogenization of polar firn and ice, *Proceedings of Symposium on Isotopes and Impurities in Snow and Ice*, IAHS-AISH Publ. **118**, 210–219 (1977a).

37. Whillans, I. M. & Grootes, P. M. Isotopic diffusion in cold snow and firn. *Journal of Geophysical Research* **90,** 3910–3918 (1985).

38. Cuffey, K. M. & Steig, E. J. Isotopic diffusion in polar firn: implications for interpretation of seasonal climate parameters in ice-core records, with emphasis on central Greenland. *Journal of Glaciology* **44,** 273–284 (1998).

39. Johnsen, S. J. *et al.* Diffusion of stable isotopes in polar firn and ice: the isotope effect in firn diffusion. Physics of ice core records, 121-140 (2000).

530 40. Gkinis, V., Simonsen, S. B., Buchardt, S. L., White, J. W. C. & Vinther, B. M. Water isotope diffusion rates
531 from the NorthGRIP ice core for the last 16,000 years – glaciological and paleoclimatic implications. *Earth and*
532 *Planetary Science Letters* **405,** 132–141 (2014).
533
534 41. Gordon, C. *et al.* The simulation of SST, sea ice extents and ocean heat transports in a version of the Hadley
535 Centre coupled model without flux adjustments. *Clim Dyn* **16,** 147–168 (2000).
536
537 42. Valdes, P. J. *et al.* The BRIDGE HadCM3 family of climate models: HadCM3@Bristol v1.0. *Geosci. Model*
538 *Dev.,* **10,** 3715-3743 (2017).
539
540 43. Berger, A. & Loutre, M. F. Insolation values for the climate of the last 10 million years. *Quaternary Science*
541 *Reviews* **10,** 297–317 (1991).
542
543 44. Spahni, R. *et al.* Atmospheric methane and nitrous oxide of the Late Pleistocene from Antarctic ice cores.
544 *Science* **310,** 1317–1321 (2005).
545
546 45. Loulergue, L. *et al.* Orbital and millennial-scale features of atmospheric CH4 over the past 800,000 years. *Nature*
547 **453,** 383–386 (2008).
548
549 46. Fogt, R. L. & Bromwich, D. H. Decadal variability of the ENSO teleconnection to the high-latitude south Pacific
550 governed by coupling with the Southern Annular Mode*. *Journal of Climate* **19,** 979–997 (2006).
551
552 47. Fogt, R. L., Bromwich, D. H. & Hines, K. M. Understanding the SAM influence on the south Pacific ENSO
553 teleconnection. *Clim Dyn* **36,** 1555–1576 (2010).
554
555 48. Schneider, D. P., Okumura, Y. & Deser, C. Observed Antarctic interannual climate variability and tropical
556 linkages. *Journal of Climate* **25,** 4048–4066 (2012).
557

558 49. Ding, Q. & Steig, E. J. Temperature change on the Antarctic Peninsula linked to the tropical Pacific*. *Journal of*
559 *Climate* **26,** 7570–7585 (2013).
560
561 50. Welhouse, L. J., Lazzara, M. A., Keller, L. M., Tripoli, G. J. & Hitchman, M. H. Composite analysis of the
562 effects of ENSO events on Antarctica. *Journal of Climate* **29,** 1797–1808 (2016).
563
564 51. Ding, Q., Steig, E. J., Battisti, D. S. & Wallace, J. M. Influence of the tropics on the Southern Annular Mode.
565 *Journal of Climate* **25,** 6330–6348 (2012).
566
567 52. Braconnot, P. *et al.* Results of PMIP2 coupled simulations of the Mid-Holocene and Last Glacial Maximum -
568 Part 2: feedbacks with emphasis on the location of the ITCZ and mid- and high latitudes heat budget. *Climate of the*
569 *Past* **3,** 279–296 (2007).
570
571 53. Abe-Ouchi, A. *et al.* Ice-sheet configuration in the CMIP5/PMIP3 Last Glacial Maximum experiments.
572 *Geoscientific Model Development Discussions* **8,** 3621-3637 (2015).
573
574 54. Ullman, D. J., LeGrande, A. N., Carlson, A. E., Anslow, F. S. & Licciardi, J. M. Assessing the impact of
575 Laurentide Ice Sheet topography on glacial climate. *Climate of the Past* **10,** 487–507 (2014).
576
577 55. Zhang, X., Lohmann, G., Knorr, G. & Purcell, C. Abrupt glacial climate shifts controlled by ice sheet changes.
578 *Nature* **512,** 290–294 (2014).
579
580 56. Zhu, J., Liu, Z., Zhang, X., Eisenman, I. & Liu, W. Linear weakening of the AMOC in response to receding
581 glacial ice sheets in CCSM3. *Geophysical Research Letters* **41,** 6252–6258 (2014).
582
583 57. Roberts, W. H. G., Valdes, P. J. & Payne, A. J. Topography's crucial role in Heinrich Events. *Proceedings of the*
584 *National Academy of Sciences* **111,** 16688–16693 (2014).
585

586 58. Di Nezio, P. N. *et al.* The climate response of the Indo-Pacific warm pool to glacial sea level. *Paleoceanography*
587 **31,** 866–894 (2016).
588
589 59. Hanebuth, T. Rapid flooding of the Sunda Shelf: A Late-Glacial sea-level record. *Science* **288,** 1033–1035
590 (2000).
591
592 60. Trenberth, K. E. *et al.* Progress during TOGA in understanding and modeling global teleconnections associated
593 with tropical sea surface temperatures. *Journal of Geophysical Research: Oceans* **103,** 14291–14324 (1998).
594
595 61. Carolin, S. A. *et al.* Varied response of western Pacific hydrology to climate forcings over the Last Glacial
596 Period. *Science* **340,** 1564–1566 (2013).
597
598 62. Yin, J. H. & Battisti, D. S. The importance of tropical sea surface temperature patterns in simulations of Last
599 Glacial Maximum climate. *Journal of Climate* **14,** 565–581 (2001).
600
601 63. Fudge, T. J. *et al.* Variable relationship between accumulation and temperature in West Antarctica for the past
602 31,000 years. *Geophysical Research Letters* **43,** 3795–3803 (2016).
603

Figure Legends

Figure 1 | WDC high-frequency signal strength

a, *The raw, high-resolution WDC δD water isotope record (grey) and a 15-yr average (red).* ***b****, Power density ratio for 15 kyr before and after the primary shift in WDC variability (i.e. 16-31 ka relative to 0-15 ka); raw data in grey and diffusion-corrected data in orange. For centennial periodicities, the mean ratio is 1.3, whereas the mean ratio for raw and diffusion-corrected periods for the 4-15 yr band is 1.9 and 2.5, respectively. The blue and green intervals show 3-7 and 4-15 yr variability, respectively. The raw data ratio is lower than one at <3 years due to increased mean diffusion in the glacial period relative to the Holocene[16]. Periods >4 years are not substantially influenced by diffusion (Extended Data Fig. 1a).* ***c, d,*** *Plots of diffusion-corrected relative amplitudes using 500-yr data windows, normalized to the most recent value, for (c) 3-7 yr variability and (d) 4-15 yr variability. Dashed lines show 1σ uncertainties (see Methods).*

Figure 2 | Indicators of oceanic and atmospheric variability

a, *Tropical Pacific-West Antarctic teleconnection strength from HadCM3 (see Fig. 3). The open red dots indicate where the teleconnection strength is 95% significantly different from the pre-industrial using a two-tailed Student's t-test.* ***b,*** *WDC diffusion-corrected 4-15 yr variability; dashed lines are 1σ uncertainties (see Methods).* ***c, d,*** *Hydrologic variability recorded in (c) an Indonesian lake sediment core[21] and (d) Bornean stalagmites[26].* ***e,*** *Relative sea level (solid line) and confidence interval (dashed lines)[28], with the estimated duration of melt water pulse (MWP) 1a[24].* ***f,*** *The NGRIP $\delta^{18}O$ record[27] from central Greenland. The dashed black line represents the ~16 ka maximum in North Atlantic ice rafted debris, corresponding to a massive freshwater discharge during H1[18]. The grey block is the estimated duration of H1[29]. The black arrow is the estimated timing of the flooding of the Sunda Shelf[21,23,24].*

Figure 3 | HadCM3 teleconnection strength

a, *Map of the correlation coefficient (R^2) for 500 hPa height and WAIS Divide δD, using the isotope enabled HadCM3 for the pre-industrial. Colors are shown for 95% statistical significance.* ***b, c, d, e*** *Composite maps of annual average 500 hPa height anomaly for ENSO events. Colors are plotted for 95% statistical significance using*

a Monte Carlo test. The green box is the Amundsen Sea region over which we calculate the teleconnection strength from the mean 500 hPa height anomaly. The purple square is the WAIS Divide ice core site. The contour interval is 5m in (b) and 2.5m in (c). Negative contours are dashed.

Figure 4 | HadCM3 Mechanistic Attribution

a, *The variance of the ASL Indices Z_{ASL} (solid line) and Z_{local} (dashed line), computed from monthly mean data that is filtered with a 4-15 yr band pass filter. The markers are unfilled if the variance of Z_{ASL} at each time slice is 95% significantly different (F-test) to that of 0 ka. At 21 ka, the orange triangle shows Z_{ASL} for 21 ka LCIS-only, and the green triangle shows Z_{ASL} for 21 ka Shelf Exposure (i.e. the effect of sea level change in the Maritime Continent region).* ***b,*** *The modeled teleconnection strength between the tropical Pacific and West Antarctica (solid red line; open red dots indicate statistically significant differences from pre-industrial).* ***c,*** *The difference in mean annual rainfall between the Central Pacific and the Maritime continent (average of 20°N-20°S, 145°E-190°E minus average of 20°N-20°S, 100°E-145°E), shown as an anomaly relative to the pre-industrial (light blue line). Also shown are the precipitation anomalies over the Maritime Continent only (dashed grey line).* ***d,*** *Northern Hemisphere ice area[30] (dashed green line) and average height of the LCIS[30] (blue line). In all panels, the dashed vertical line shows 16 ka, as in Figure 2.* ***e,*** *Map of the change in the 500 hPa height field variance between 21 ka and the pre-industrial.* ***f,*** *As in (e), except for the Z_{pac} variability that is linearly related to ENSO (i.e. the part removed from Z_{ASL} to yield Z_{local}). The green box is the Amundsen Sea region over which we calculate the ASL Indices in (a). The purple square is the WAIS Divide ice core site. The contour interval is 40 m^2, with colors changing every 80 m^2. Negative contours are dashed. Colors are plotted for 95% statistical significance using a Monte Carlo test.*

Extended Data Figure Legends

Extended Data Figure 1 | Signal Detection

a, *Relative amplitudes for 1-yr, 2-yr, 3-yr, and 4-yr periods calculated for 500-yr spectral data windows, normalized to the value for the annual signal in the most recent data window. Both the climate and diffusion affects the amplitude of these high-frequency signals. However, it is mainly the effects of diffusion that cause the loss of the annual signal at >14 ka. Similarly, the 2-yr period is lost between ~17-19 ka, when the rate of diffusion for WDC was highest[16]. Periods >3 yrs survive diffusion throughout the last 31 kyr.* ***b,*** *An example of a deconvolution calculation showing the observed δD water isotope record (i.e raw data; dotted red line), and the diffusion-corrected record (black line). While this calculation was not used for the data presented in this paper, it serves as a visual aide in understanding how the diffusion-corrected water isotope record would look in the time-domain. We performed all diffusion-correction calculations in the frequency domain to reduce uncertainty.* ***c,*** *The power density spectrum for the SOI Index from 1951-2017 (black; 95% confidence intervals in grey), compared with a red noise null hypothesis (red) calculated from the average of 100 power spectrums of synthetic data that have the same autocorrelation and variance as the SOI. The SOI has power greater than the red noise across a broad spectral peak between ~2-17 yrs, which can be subdivided into a ~2-7 yr high frequency peak and an ~8-17 yr peak. Due to the limited temporal span of modern observations, multi-decadal spectral estimates of the SOI cannot be adequately defined.* ***d,*** *Diffusion-corrected relative amplitudes using 500-yr windows of WDC water isotope data.* ***e,*** *The difference in age of consecutive 5 mm WDC water isotope samples (Δage_{5mm}; blue) and a 500-yr sliding average (red).* ***f,*** *The WDC accumulation rate[63], inverted. The accumulation, and by extension the Δage_{5mm} in (e), undergoes large changes during the deglaciation at ~18.5 ka, occurring 2.5 millennia before the change point in teleconnection strength at ~16 ka.*

Extended Data Figure 2 | Change Point Detection

a, *WDC 4-15 yr variability for 500-yr data windows (dashed lines are 1σ uncertainties; see Methods).* ***b,*** *Regression test algorithm to determine the first significant change in the WDC 4-15 yr variability in (a). The first colored data point below the p-value significance threshold occurs at 16.44 ka.* ***c,*** *Example of the diffusion-correction calculation for a 100-yr data window centered on 15.54 ka bp; raw data (black), diffusion corrected data (blue), Gaussian fit*

(red) with dashed 1σ uncertainty bounds (see Methods). The same calculation is made for 500-yr data windows. ***d,*** *The sub-set of diffusion-corrected 4-15 yr amplitudes (green) calculated at 100-yr resolution. The values are normalized to the amplitude value at 16.24 ka, which represents the change point towards smaller amplitudes.*

Extended Data Figure 3 | ASL variability

Panels (a) and (b) show the variance of the ASL Indices Z_{ASL} (black) and Z_{local} (blue). ***a,*** *The ASL Indices are computed from monthly mean data then filtered with a 4-15 yr band pass filter.* ***b,*** *The ASL Indices are computed from annual mean output. We compute Z_{ASL} as the mean 500 hPa height in the region 55°-70°S and 195°-240°E. The blue lines show Z_{ASL} after linearly removing the SST_{pac} time series from the 500 hPa height field; this is the ASL variability unrelated to the tropical Pacific (Z_{local}; see Methods). The markers are unfilled if the variance of Z_{ASL} at each time slice is 95% significantly different (F-test) to that of the pre-industrial.* ***c,*** *Map of the change in the variance of the 500 hPa height field between 21 ka and the pre-industrial.* ***d,*** *The variability that is linearly related to ENSO, Z_{pac} (this is the part removed from Z_{ASL} to yield Z_{local}).* ***e,*** *The variability with the effect of ENSO linearly removed (see Methods; this the equivalent of Z_{local}). Changes not attributable to ENSO occur to the north of the Amundsen Sea, while changes over the Amundsen Sea are related to ENSO. In (c), (d), and (e) the contour intervals are 40 m^2, with colors changing every 80 m^2. Negative contours are dashed.*

Extended Data Figure 4 | Composites of the 500 mb height field for ENSO events

Composites for ***a,*** *the pre-industrial,* ***b,*** *Full 21ka, and* ***c,*** *the difference between Full 21ka and pre-industrial. Colors are plotted for 95% statistical significance using a Monte Carlo test. Negative contours are dashed. In (a) and (b) the contours are plotted every 5 m and colors saturate at ±25 m. The thin blue box shows where the ASL index is computed. In (c) contours are plotted every 2.5 m and colors saturate at ±12.5 m.*

Extended Data Figure 5 **| Tropical Pacific-to-ASL teleconnection strength**

Computed using the Full 28-0 ka simulations. ***a,*** *Average 500 hPa geopotential height anomaly in the Amundsen Sea region, computed within the blue box shown in Extended Data Figure 4. These values are derived from composites constructed using only the lower limits on the size of ENSO events (see Main Text and Methods).* ***b,*** *The t-score is shown by the red line. Values outside the shaded red region are 95% statistically different from the pre-industrial.*

Extended Data Figure 6 | Composites of the 500mb height field for ENSO events with and without upper bound ***a,*** *The teleconnection without upper limit using the Full 21 ka simulation.* ***b,*** *The teleconnection with upper limit using the Full 21 ka simulation.* ***c,*** *The difference in teleconnection between the Full 21ka simulation and the pre-industrial without upper limit.* ***d,*** *The same difference as (c) with upper limit. In all panels, negative contours are dashed, and colors are plotted for 95% statistical significance using a Monte Carlo test. In (a) and (b), the contours are plotted every 5 m and colors saturate at ±25 m. In (c) and (d), contours are plotted every 2.5 m and colors saturate at ±12.5 m.*

Extended Data Figure 7 | Composite maps of annual average 500mb height inPMIP2/3 models

For each model the top panel shows the 0 ka composite and the bottom panel the difference between the Full 21 ka and 0 ka simulation. Colors are plotted for 95% statistical significance using a Monte Carlo test. In the upper panels, contours are plotted at 5m intervals, with colors saturating at 25m. In the lower panels contours are plotted at 2.5m intervals, with colors saturating at ±12.5 m. Negative contours are dashed. The reduced statistical significance in these panels compared to those shown in Extended Data Figures 4, 6, 8, 9, and 10 is due to the shorter data series available in the PMIP2/3 archives.

Extended Data Figure 8 | Sensitivity of composite maps to different sets of 21ka boundary conditions

All plots show the difference between 21ka and 0ka composites. The composites are constructed using both upper and lower limits on the size of ENSO events. Contours are plotted every 2.5 m (negative contours are dashed) and colors saturate at ±12.5 m. Colors are plotted for 95% statistical significance using a Monte Carlo test. ***a,*** *Full 21 ka simulation.* ***b,*** *21 ka orbit + GHG.* ***c,*** *21 ka ice sheets.* ***d,*** *21 ka West Pacific shelf exposure.* ***e,*** *21 ka LCIS albedo + topography, (where LCIS is the combined Laurentide-Cordilleran ice sheets).* ***f,*** *21 ka LCIS albedo. Each of these simulations is fully defined in the Supplementary Information Data spreadsheet.*

Extended Data Figure 9 | Annual mean anomalies of precipitation and sea surface temperature

Maps of 21 ka anomalies relative to the pre-industrial. ***a,*** *Full 21 ka simulation.* ***b,*** *21 ka ice sheets.* ***c,*** *21 ka LCIS albedo + topography.* ***d,*** *21 ka West Pacific shelf exposure. Annual means are calculated from 100 years of output.*

737 *Contour intervals for precipitation are 1 mm day^{-1}, and for sea surface temperature are 0.5°C. Land areas are*

738 *shown in in grey. Note that the temperature color scale in (a) ranges from -4 to 0 °C. This accounts for the mean*

739 *GHG cooling that is seen in the Full 21 ka simulation.*

740

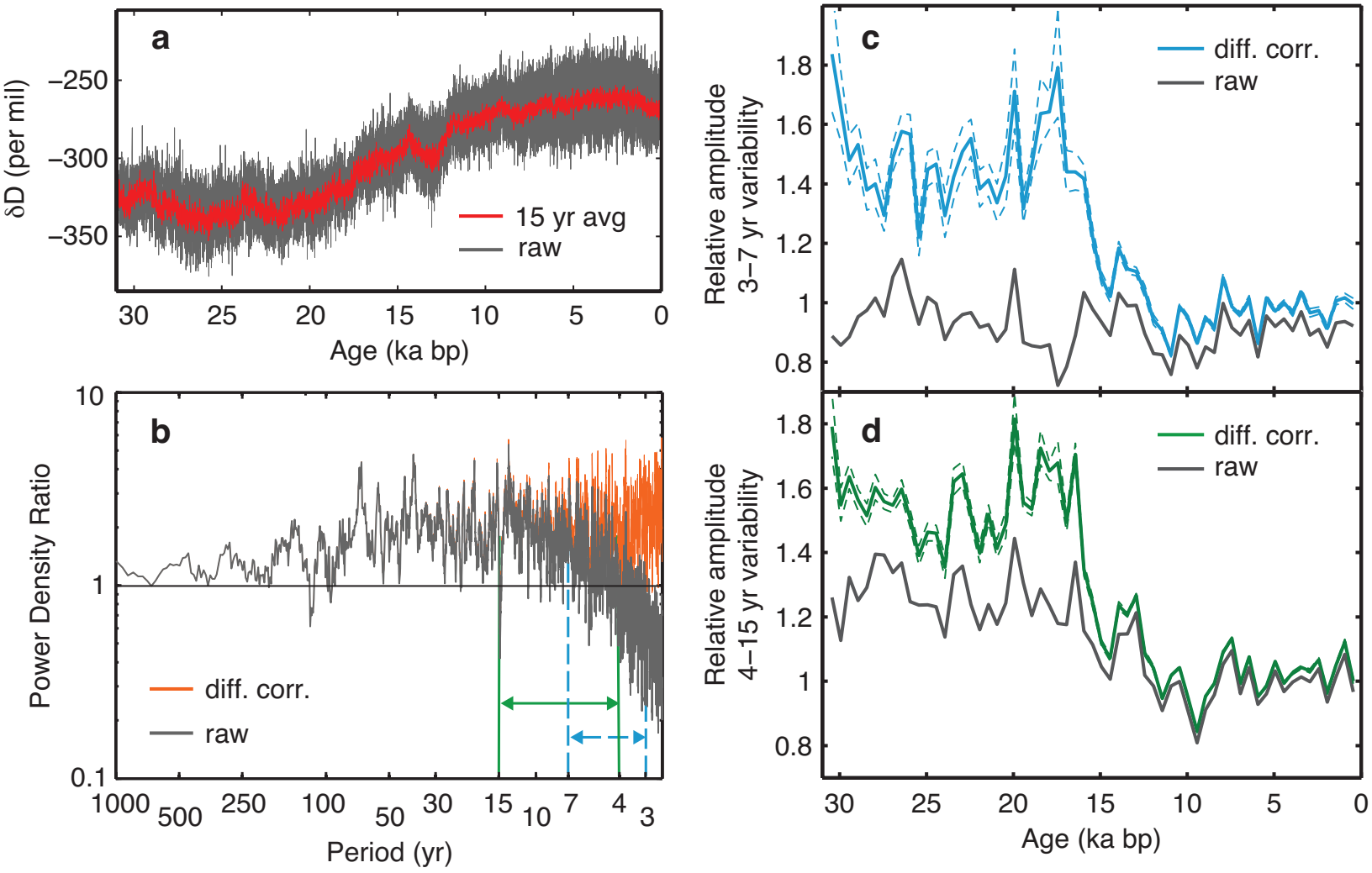
a
δD (per mil)
−250
−300
−350
15 yr avg
raw
30
25
20
15
10
5
0
Age (ka bp)
b
Power Density Ratio
10
1
0.1
diff. corr.
raw
1000
500
250
100
50
30
15
10
7
4
3
Period (yr)
c
Relative amplitude
3–7 yr variability
1.8
1.6
1.4
1.2
1
0.8
diff. corr.
raw
d
Relative amplitude
4–15 yr variability
1.8
1.6
1.4
1.2
1
0.8
diff. corr.
raw
30
25
20
15
10
5
0
Age (ka bp)

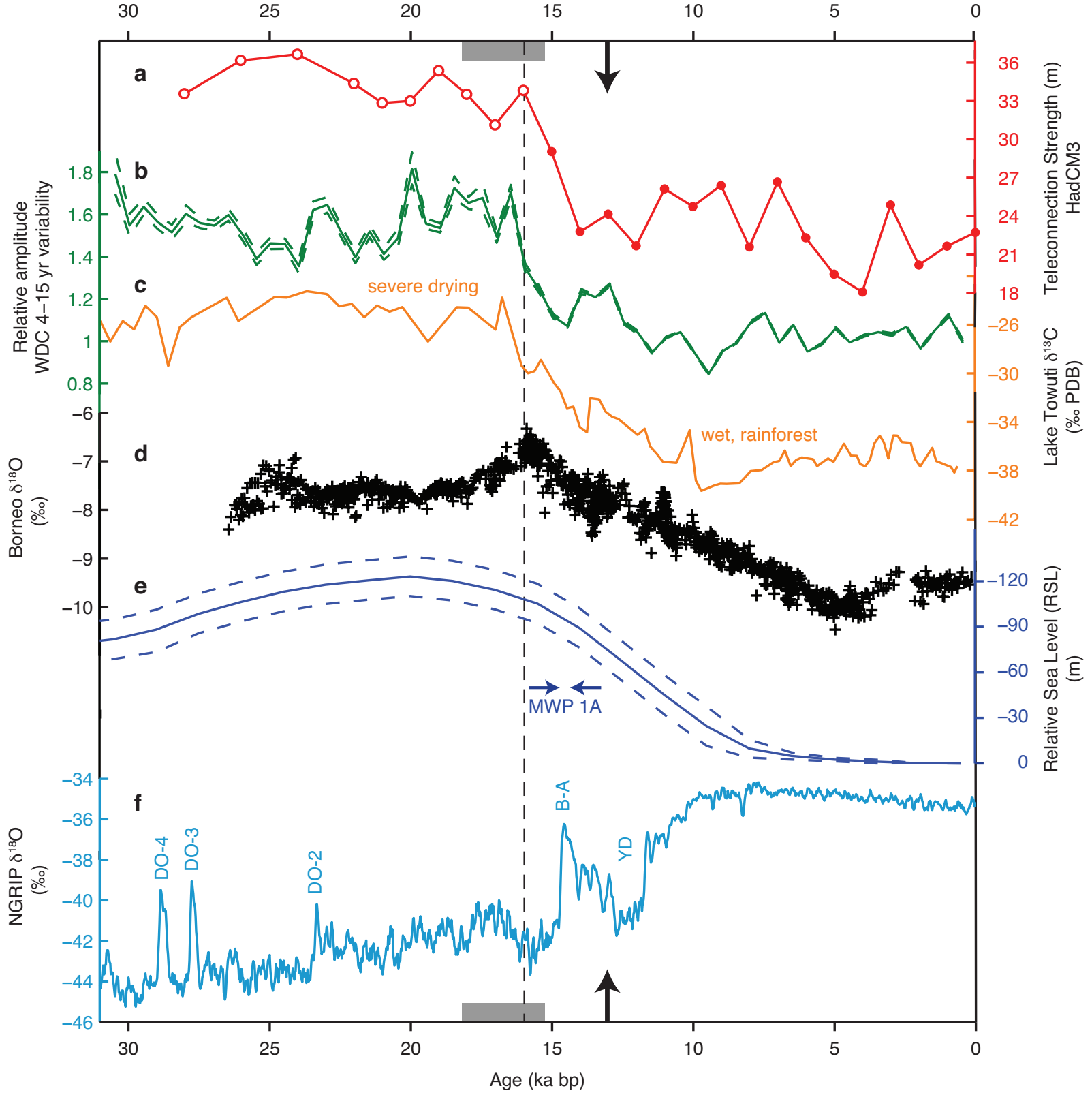
a
b
c
d
e
f
severe drying
wet, rainforest
MWP 1A
DO-4
DO-3
DO-2
B-A
YD
Relative amplitude
WDC 4–15 yr variability
Teleconnection Strength (m)
HadCM3
Lake Towuti δ13C
(‰ PDB)
Borneo δ18O
(‰)
Relative Sea Level (RSL)
(m)
NGRIP δ18O
(‰)
Age (ka bp)

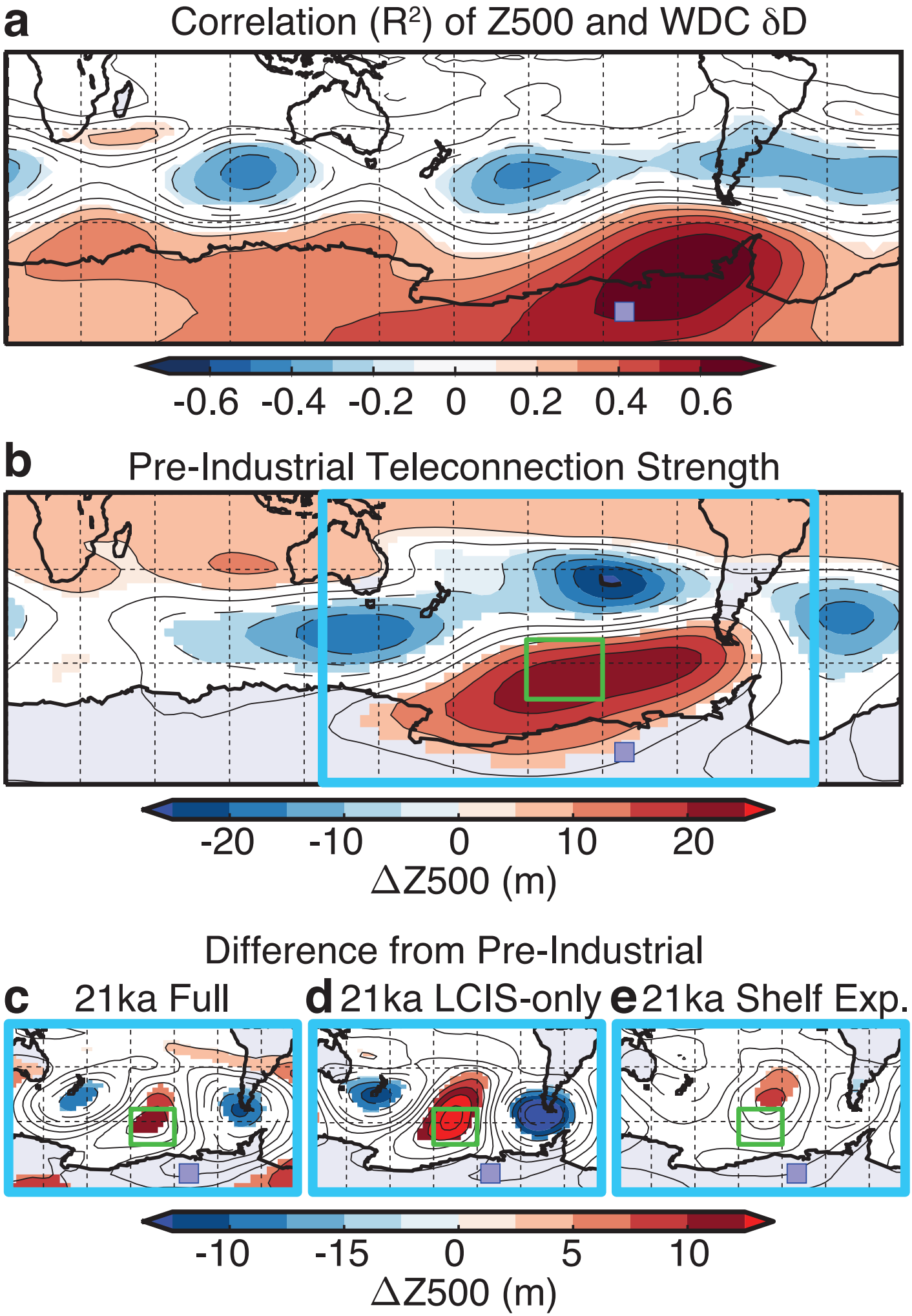
a
Correlation (R²) of Z500 and WDC δD
-0.6 -0.4 -0.2 0 0.2 0.4 0.6
b
Pre-Industrial Teleconnection Strength
-20 -10 0 10 20
ΔZ500 (m)
Difference from Pre-Industrial
c 21ka Full
d 21ka LCIS-only
e 21ka Shelf Exp.
-10 -15 0 5 10
ΔZ500 (m)

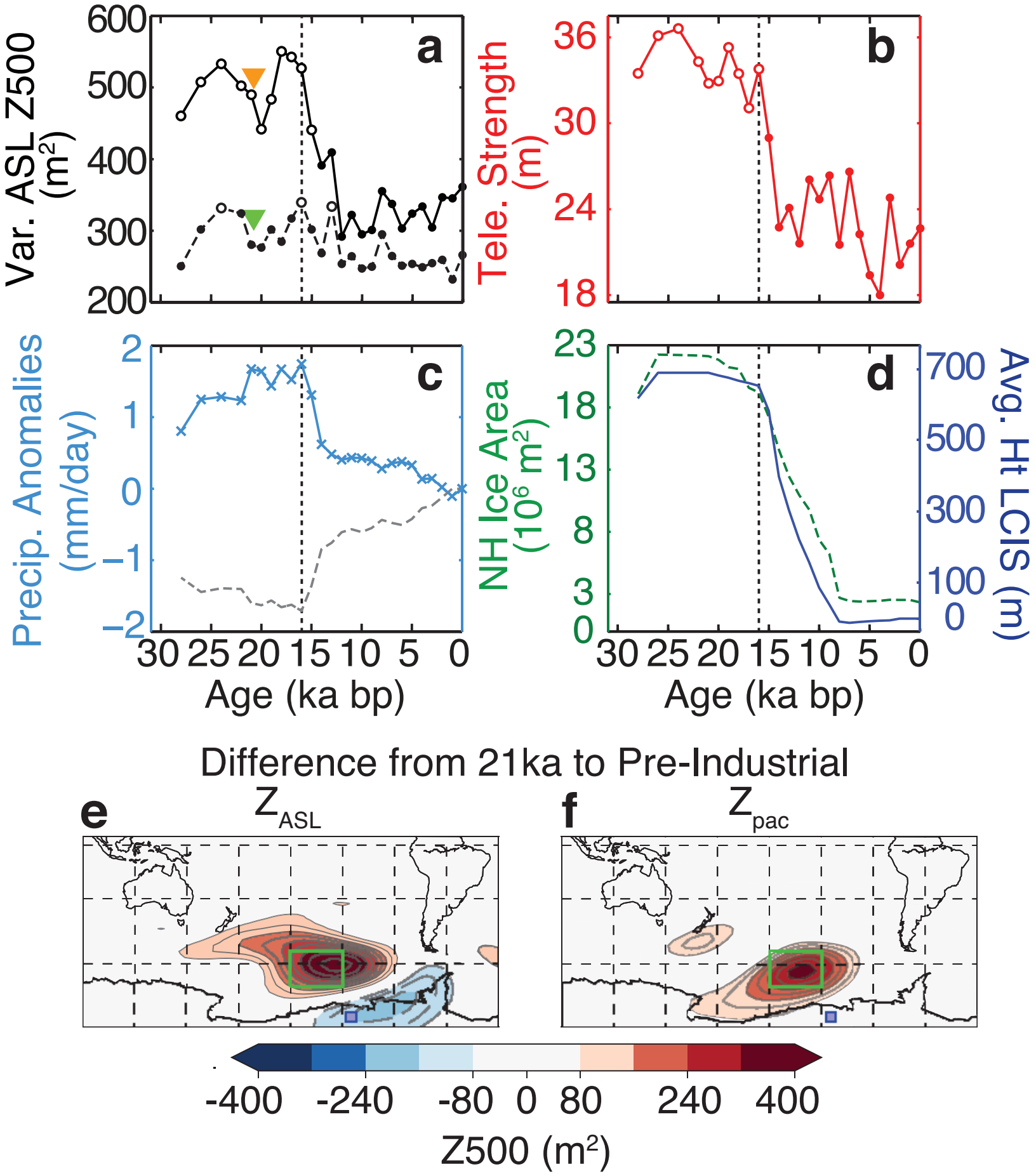
a
b
c
d
Var. ASL Z500 (m²)
Tele. Strength (m)
Precip. Anomalies (mm/day)
NH Ice Area (10⁶ m²)
Avg. Ht LCIS (m)
Age (ka bp)
Age (ka bp)
Difference from 21ka to Pre-Industrial
e
Z_ASL
f
Z_pac
-400 -240 -80 0 80 240 400
Z500 (m²)